Energetic Submesoscales Maintain Strong Mixed Layer Stratification during an Autumn Storm

DANIEL B. WHITT

National Center for Atmospheric Research, Boulder, Colorado

JOHN R. TAYLOR

Department of Applied Mathematics and Theoretical Physics, University of Cambridge, Cambridge, United Kingdom

ABSTRACT

Atmospheric storms are an important driver of changes in upper-ocean stratification and small-scale (1–100 m) turbulence. Yet, the modifying effects of submesoscale (0.1–10 km) motions in the ocean mixed layer on stratification and small-scale turbulence during a storm are not well understood. Here, large-eddy simulations are used to study the coupled response of submesoscale and small-scale turbulence to the passage of an idealized autumn storm, with a wind stress representative of a storm observed in the North Atlantic above the Porcupine Abyssal Plain. Because of a relatively shallow mixed layer and a strong downfront wind, existing scaling theory predicts that submesoscales should be unable to restratify the mixed layer during the storm. In contrast, the simulations reveal a persistent and strong mean stratification in the mixed layer both during and after the storm. In addition, the mean dissipation rate remains elevated throughout the mixed layer during the storm, despite the strong mean stratification. These results are attributed to strong spatial variability in stratification and small-scale turbulence at the submesoscale and have important implications for sampling and modeling submesoscales and their effects on stratification and turbulence in the upper ocean.

1. Introduction

The upper ocean, particularly at midlatitudes, is subject to intense, highly variable winds associated with synoptic atmospheric storms. These intermittent events energize nearly isotropic turbulence at length scales smaller than the mixed layer depth, which drives entrainment and mixing of pycnocline water into the mixed layer and thereby deepens the mixed layer and increases its density (e.g., Davis et al. 1981; Large and Crawford 1995; Dohan and Davis 2011; Forryan et al. 2015). In aggregate, storm-driven, small-scale turbulence contributes significantly to the seasonal increase in the mixed layer depth and mixed layer density during the autumn in midlatitudes (e.g., Large et al. 1986). Many previous studies have examined the upper-ocean response to storms using a one-dimensional framework (e.g., Pollard et al. 1972; Niiler and Kraus 1977; Price et al. 1978; Large et al. 1994). However, the upper ocean contains lateral variability associated with large-scale fronts, filaments, and eddies, which modify the evolution of upper-ocean stratification and small-scale turbulence during a storm.

Among the motions inducing lateral variability are submesoscales, anisotropic features with vertical scales similar to the mixed layer, horizontal scales between 0.1 and 10 km, and $O(1)$ vorticity Rossby numbers (e.g., Thomas et al. 2008; Capet et al. 2008; McWilliams 2016), which are prevalent in the upper ocean (e.g., Munk et al. 2000; Shcherbina et al. 2013; Buckingham et al. 2016; Thompson et al. 2016). Submesoscales play an important role in restratifying the mixed layer (e.g., Haine and Marshall 1998; Lapeyre et al. 2006; Boccaletti et al. 2007; Mahadevan et al. 2010, 2012) and enhancing the exchange of water between the mixed layer and pycnocline (e.g., Lévy et al. 2001; Klein and Lapeyre 2009; Thomsen et al. 2016). In addition, submesoscales modify the energetics and fluxes associated with small-scale turbulence in the mixed layer (e.g., D'Asaro et al. 2011; Smith et al. 2016; Taylor 2016). For example, submesoscales transfer energy from large-scale geostrophic

Corresponding author: Daniel B. Whitt, dwhitt@ucar.edu

gradients to small-scale turbulence, while submesoscale stratification in the mixed layer locally inhibits turbulence.

Many submesoscale features are spawned from instabilities associated with horizontal density gradients or fronts (e.g., Haine and Marshall 1998; Boccaletti et al. 2007; Callies et al. 2016). These instabilities can be interpreted via stability analysis of an "Eady-like" baroclinic zone with parameters characteristic of the mixed layer (e.g., Stone 1966; Stamper and Taylor 2016). Depending on the gradient Richardson number Ri_g associated with the vertically sheared balanced flow, the fastest growing mode is one of two types: mixed layer baroclinic instability (MLI; when $\text{Ri}_g > 0.95$) or symmetric instability (SI; when $\text{Ri}_g < 0.95$). The most unstable normal mode of MLI is invariant in the cross-front direction and converts available potential energy associated with tilting isopycnals into kinetic energy and ultimately submesoscale eddies, while SI is invariant in the alongfront direction and draws its energy from the vertical shear. The net effect of both instabilities is to lower the center of mass of the fluid and increase the stable stratification in the mixed layer. However, submesoscales in the real ocean are a chaotic, nonlinearly interacting continuum rather than a discrete set of linear modes (e.g., Shcherbina et al. 2013).

Many of the numerical simulations upon which our understanding of nonlinear/turbulent submesoscale dynamics is based have either been unforced initial-value problems (e.g., Özgökmen et al. 2011; Skyllingstad and Samelson 2012; Stamper and Taylor 2016) or forced with steady surface cooling or winds (e.g., Taylor and Ferrari 2010; Thomas et al. 2013; Hamlington et al. 2014; Taylor 2016). One exception is a study of a storm event at the Gulf Stream front using observations and large-eddy simulations (LES) reported in Thomas et al. (2016). They found turbulent dissipation rates in excess of anticipated values and rapid restratification of the boundary layer and attributed these features to SI. Although they captured SI, the simulations in Thomas et al. (2016) had a limited domain size that excluded the possibility of MLI and hence submesoscale eddies.[1]

Despite the attention paid to submesoscales in recent years, the response of submesoscale eddies to storms is not well understood. Basic open questions remain, including the following: Can MLI maintain a stable stratification during intense storms? Are submesoscale

eddies damped by small-scale turbulent mixing associated with strong winds? How is the small-scale turbulence in the mixed layer influenced by submesoscales during storms?

We address these questions using high-resolution LES, motivated by observations collected near 48.7°N, 16.3°W above the Porcupine Abyssal Plain during the Ocean Surface Mixing, Ocean Submesoscale Interaction Study (OSMOSIS), which reveal significant submesoscale activity throughout the year (Thompson et al. 2016; Buckingham et al. 2016). On 24–26 September 2012, during the deployment cruise, a storm passed over the field site and deepened the mixed layer (Rumyantseva et al. 2015). Glider profiles collected during the storm show that the mixed layer remained well stratified throughout the storm (their Fig. 4). An idealized representation of this event will be the basis for our analysis.

2. Model description

To elucidate the interaction between submesoscales and small-scale turbulence during the life cycle of a storm, we present results from a simulation in a large domain that captures the fastest growing MLI length scale, hence the associated energy source for submesoscale eddies, while simultaneously resolving small-scale turbulence. The domain is 1970 m by 1970 m by 80 m covered by a grid with 1024 by 1024 by 160 points that achieves a uniform resolution of 1.9 m by 1.9 m by 0.5 m in x and y and z, respectively. As in Taylor and Ferrari (2010) and Taylor (2016), the flow is expressed as a periodic (in x and y) perturbation from a fixed/constant mean horizontal density gradient $\langle M^2 \rangle_{x,y} = \langle (g/\rho_0)(\partial\rho/\partial y) \rangle_{x,y} = 5 \times 10^{-8}\,\text{s}^{-2}$ and thermal wind shear $\langle M^2 \rangle_{x,y}/f = 5 \times 10^{-4}\,\text{s}^{-1}$ that are representative of the OSMOSIS site before the storm (C. Buckingham 2017, personal communication). Here, ρ is the density, $\rho_0 = 1026\,\text{kg m}^{-3}$ is the reference density, g is the acceleration caused by gravity, the Coriolis frequency $f = 10^{-4}\,\text{s}^{-1}$, and $\langle \cdot \rangle_{x,y}$ denotes a horizontal average.

The turbulent state at the onset of the storm (Fig. 1a) is obtained from a 3-day spinup simulation (Whitt 2017) that is forced by a constant air–sea (i.e., surface) buoyancy flux $B_A = 3 \times 10^{-9}\,\text{m}^2\,\text{s}^{-3}$ (buoyancy $b = -g\rho/\rho_0$ is simulated, but this is roughly equivalent to a heat loss of $10\,\text{W m}^{-2}$ to the atmosphere) and initialized with low-amplitude red noise on a vertical density profile based on Fig. 3b of Rumyantseva et al. (2015). The mixed layer depth H_{ML}, which is defined by an increase in the mean density $\langle\rho\rangle_{x,y}$ by $0.03\,\text{kg m}^{-3}$ relative to the surface, is initially 35 m. The mixed layer is stratified: $\langle N^2 \rangle_{x,y} = \langle -(g/\rho_0)(\partial\rho/\partial z) \rangle_{x,y} = 2.5 \times 10^{-7}\,\text{s}^{-2}$, and the initial balanced Richardson number $\text{Ri}_B = f^2\langle N^2 \rangle_{x,y}/ \langle M^2 \rangle_{x,y}^2 = 1$. In the pycnocline, $\langle N^2 \rangle_{x,y} = 3.5 \times 10^{-4}\,\text{s}^{-2}$ and $\text{Ri}_B = 1400$. The fastest growing MLI mode has a horizontal

---

[1] Skyllingstad et al. (2017), which was accepted for publication after the submission of this paper, present several large-eddy simulations of wind-forced fronts, expanding on Thomas et al. (2016). However, the analysis also focuses on domains that are too small to permit MLI.
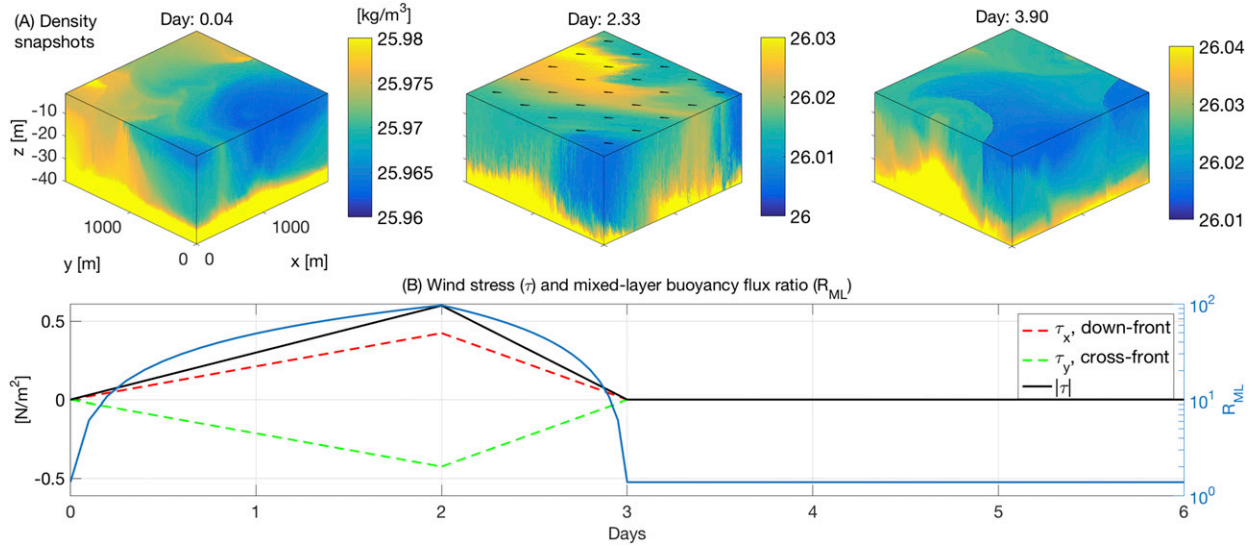
FIG. 1. (a) Snapshots of density and (b) time series of wind stress magnitude (black) and vector components (dashed red and green) as well as the mixed layer buoyancy flux ratio R_{ML} (blue) [see (1)]. Black vectors in the snapshot at day 2.33 indicate the direction of the wind during the storm.

scale $L_{\mathrm{MLI}} = [(2\pi \langle M^2 \rangle_{x,y} H_{\mathrm{ML}})/f^2] \sqrt{(2 + 2\mathrm{Ri}_B)/5} \approx 985$ m (Stone 1966), which is half the domain size. The growth time scale of this mode is $T_{\mathrm{MLI}} = (3.3/|f|)\sqrt{\mathrm{Ri}_B + 1} \approx 13$ h.

The storm forcing during 24–26 September 2012 at the OSMOSIS site is represented by the idealized spatially uniform but time-dependent surface stress in Fig. 1b, which points 45° to the right of the mean geostrophic flow at the surface. Following the storm, the simulations continue for about 4 days without wind stress to elucidate the subsequent adjustment and restratification. To separate the effects of storm winds from storm buoyancy fluxes, the air–sea buoyancy flux is held constant at $B_A = 3 \times 10^{-9}\,\mathrm{m^2\,s^{-3}}$ during and after the simulated storm; this B_A is about 10 times weaker than the buoyancy flux associated with the observed cooling during the storm (Rumyantseva et al. 2015).

To separate the influence of the front and submesoscales from the classic "one-dimensional" effects of the wind stress on the small-scale turbulence and stratification, the wind-forced simulation in the large domain is compared to a simulation in a small domain without a front or submesoscales. The small domain is 492.5 m by 492.5 m by 80 m and has the same grid resolution, the same surface boundary conditions, and the same mean density profile $\langle \rho \rangle_{x,y}(z)$ at day 0 as the large domain, but $\langle M^2 \rangle_{x,y} = 0$.

To identify how the wind modifies the submesoscales, two additional simulations are carried out in the large domain with $\langle M^2 \rangle_{x,y} = 5 \times 10^{-8}\,\mathrm{s^{-2}}$. These simulations are identical to the baseline simulation described above except that they are forced only by an air–sea buoyancy flux and the surface stress is zero. In the first of the additional simulations, the buoyancy flux $B_A = 3 \times 10^{-9}\,\mathrm{m^2\,s^{-3}}$ is

weak and constant, as in the wind-forced simulation. In the second simulation, the buoyancy flux is strong and time dependent; it takes the same magnitude as the Ekman buoyancy flux in the wind-forced simulation, that is $B_A = \mathrm{EBF} = (\tau_x \langle M^2 \rangle_{x,y})/(\rho_0 f)$ (see Fig. 1b). Prior work has suggested that the relative strength of the competing destratifying Ekman and air–sea buoyancy fluxes and restratifying submesoscale buoyancy flux can be quantified using the mixed layer buoyancy flux ratio:

$$R_{\mathrm{ML}} = \frac{B_A + \mathrm{EBF}}{B_{\mathrm{MLI}}}, \qquad (1)$$

where the submesoscale buoyancy flux $B_{\mathrm{MLI}} = 2.1 \times 10^{-9}\,\mathrm{m^2\,s^{-3}}$ is a constant derived from a parameterization of MLI, assuming a constant mixed layer depth of 37.5 m (Fox-Kemper et al. 2008; Mahadevan et al. 2010, 2012). Here, R_{ML} is between 10 and 100 during the storm and $R_{\mathrm{ML}} = 1.4$ before and after the storm (Fig. 1b). Both the wind and strong buoyancy flux–forced fronts have the same R_{ML}.

All simulations are carried out with DIABLO (Taylor 2008), which solves the discrete, incompressible Boussinesq equations using a pseudospectral method for horizontal derivatives and second-order finite differences for vertical derivatives. Time stepping is accomplished using a third-order Runge–Kutta scheme for advection and the implicit Crank–Nicholson scheme for viscosity/diffusion. The LES solves a filtered version of the governing equations, which are closed using a modified Smagorinsky model to represent subgrid-scale stresses (Kaltenbach et al. 1994). The subgrid-scale
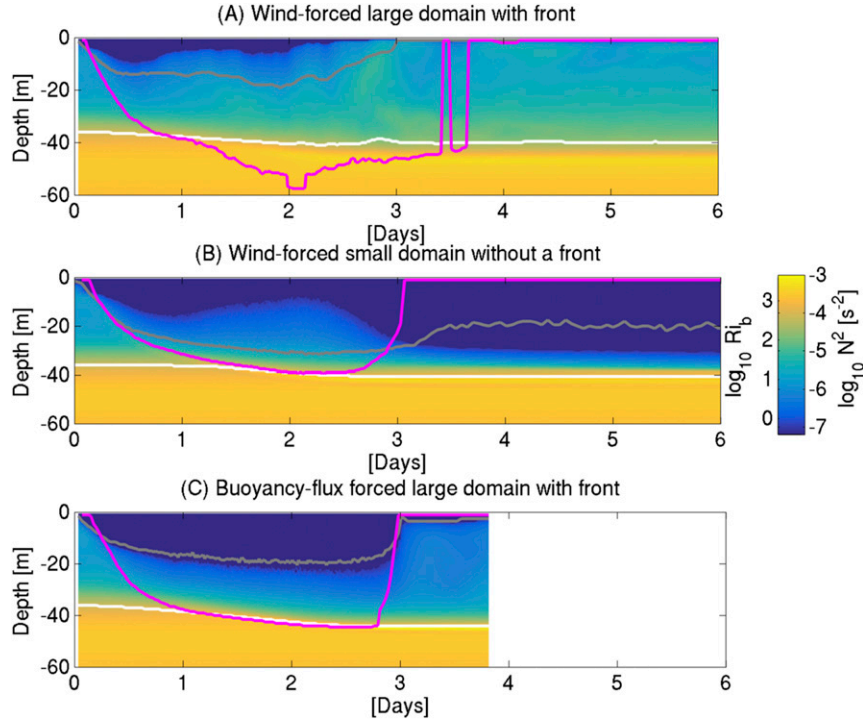
FIG. 2. Time series of horizontally averaged stratification $\langle N^2 \rangle_{x,y}$ and (equivalently) the balanced Richardson number $\mathrm{Ri}_B = f^2 \langle N^2 \rangle_{x,y} / \langle M^2 \rangle_{x,y}^2$ in three simulations: (a) the wind-forced front, (b) the wind-forced domain without a front, and (c) the strong buoyancy flux–forced front. Panels also include time series of mixed layer depth H_{ML} (white), mixing layer depth H_{XL} (magenta), and the low-gradient Richardson number depth H_{Ri} (gray), above which the gradient Richardson number $\mathrm{Ri}_g \lesssim \frac{1}{4}$.

diffusivity $\kappa_{\mathrm{SGS}} = \nu_{\mathrm{SGS}} \mathrm{Pr}_{\mathrm{SGS}}^{-1}$ depends on the subgrid-scale viscosity ν_{SGS} and the subgrid-scale Prandtl number, which is parameterized in terms of the gradient Richardson number at the grid scale $\mathrm{Ri}_{\mathrm{GS}} = (-g/\rho_0)(\Delta\rho\Delta z)/(\Delta u^2 + \Delta v^2)$, that is, $\mathrm{Pr}_{\mathrm{SGS}}^{-1} = 1/(1 + \mathrm{Ri}_{\mathrm{GS}}/0.94)^{1.5}$ (as in Anderson 2009), where u, v are the horizontal velocities, and Δ indicates the difference between two vertically adjacent grid cells.

3. Results

At the onset of the storm, the density variance in the mixed layer of the large domain is dominated by submesoscales, although the domain contains variability at all resolved scales (Fig. 1a). In addition, submesoscale density variability remains a dominant feature of the mixed layer both during and after the storm. The following sections describe the simulated evolution of the mean stratification and small-scale turbulence as well as submesoscale variability within the mixed layer during and after the storm.

a. Mean stratification, shear, and dissipation

Both during and after the storm, the mixed layer is characterized by a stronger mean stratification $\langle N^2 \rangle_{x,y}$

and a higher-gradient Richardson number $\mathrm{Ri}_g = \langle N^2 \rangle_{x,y} / (\langle \partial u/\partial z \rangle_{x,y}^2 + \langle \partial v/\partial z \rangle_{x,y}^2)$ in the wind-forced front than in the wind-forced domain without a front or the strong buoyancy flux–forced front (Fig. 2). The stronger stratification implies a higher balanced Richardson number $\mathrm{Ri}_B = f^2 \langle N^2 \rangle_{x,y} / \langle M^2 \rangle^2$, which indicates the mean balanced flow is more stable to some classes of instability; $\mathrm{Ri}_B > 1$ indicates symmetric stability, and $\mathrm{Ri}_B > 0$ indicates gravitational stability. In both simulations with a front, the mean state is stable to gravitational instability ($\mathrm{Ri}_B > 0$) and Kelvin–Helmholtz instability ($\mathrm{Ri}_g > \frac{1}{4}$) throughout much of the mixed layer, despite strong surface momentum or buoyancy fluxes, in contrast to the wind-forced domain without a front.

Despite the strong mean stratification and higher Ri_B throughout much of the mixed layer, the mixing layer depth H_{XL}, where the dissipation rate $\langle \varepsilon \rangle_{x,y} > 10^{-8}\,\mathrm{W\,kg^{-1}}$, is deeper during the storm in the wind-forced front compared to the wind-forced domain without a front or the front forced by a strong air–sea buoyancy flux. In addition, H_{XL} remains deeper than H_{ML} for 0.5 days after the storm is over in the wind-forced front, unlike the other two strongly forced simulations (Fig. 2).
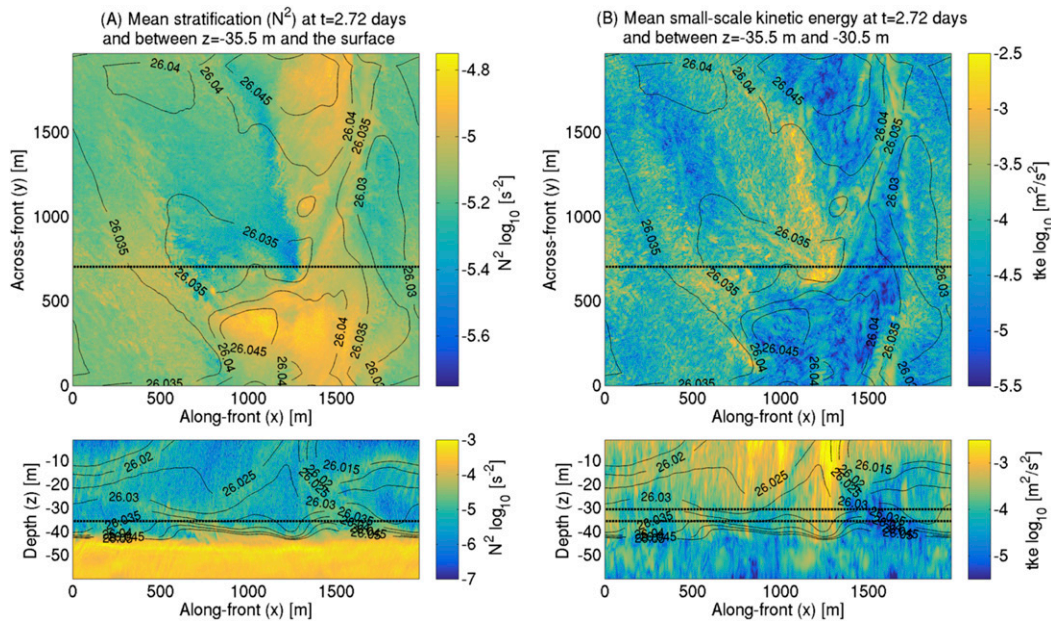
FIG. 3. Snapshots of (a) stratification N^2 and (b) small-scale turbulent kinetic energy at $t = 2.72$ days in the wind-forced front (just before the end of the storm, see Fig. 1b). Solid black contours of the large-scale density are overlaid. (top) The x–y slices are calculated as an average from $z = -35.5$ m to the surface in (a) and from $z = -35.5$ to -30.5 m in (b). (bottom) The x–z slices are calculated at the y location indicated by the dashed black lines in the x–y slices. Here, large scales are defined by applying a 150 m by 150 m square filter to the full fields at each vertical level, while small scales are defined as the difference between the full fields and the large-scale fields.

b. Spatial variability

The combination of a strongly stratified and turbulent mixing layer is paradoxical, but it can be explained by spatial variability associated with submesoscales. Both during and after the storm, the stratification N^2 in the wind-forced front exhibits submesoscale variations of one to two orders of magnitude within the mixed layer at all depths (Figs. 3a, 4a). Regions of high stratification $N^2 \gtrsim 10^{-5} \, \text{s}^{-2}$, which dominate the horizontal average, are associated with high potential vorticity, which is much greater than 0, but regions of low stratification are associated with negative potential vorticity (not shown). Hence, the criteria for SI are met locally in some regions of the domain (Hoskins 1974), but the high mixed layer stratification cannot be explained by SI, which tends to restore unstable regions with potential vorticity of the opposite sign of f toward conditions neutral to SI with zero potential vorticity and $\text{Ri}_B \simeq 1$ (e.g., Taylor and Ferrari 2010; Thomas et al. 2013, 2016). This contrasts with the wind-forced front presented here, where $\text{Ri}_B \sim 10$ to 100 in the mixed layer during the storm (Fig. 2a), much larger than the neutral state for SI.

During the storm, the submesoscale variability lacks clear, coherent, vortical structures, but as the storm subsides, a coherent submesoscale cyclonic

vortex quickly develops and can be seen by day 3.0 (snapshots at day 3.3 are shown in Fig. 4a). This vortex, which has a strongly stratified core and weakly stratified edges, qualitatively dominates the submesoscale variability after the storm (Fig. 4a). The vortex diameter is quantitatively consistent with the fastest growing MLI length scale (about 1 km), and it emerges on a time scale that is quantitatively consistent with the fastest growing MLI time scale (about half a day). However, the vortex forms during the storm and its growth may be significantly modified by the wind and the associated ageostrophic shear.

The small-scale (<150 m) turbulent kinetic energy exhibits spatial variations of one to two orders of magnitude within the mixed layer during and after the storm, and the pattern of variability of small-scale turbulence is qualitatively similar to the variability in stratification. As a result, strong turbulence penetrates to the mixed layer base in only a small fraction of the domain. Yet, this variability is sufficient to explain why the mixing layer depth H_{XL}, defined using $\langle \varepsilon \rangle_{x,y}$ in Fig. 2a, penetrates deeply into the region of strong mean stratification. The cause of these deep penetrating events is not known but could be due to local interactions between the wind and the submesoscale fronts and filaments.
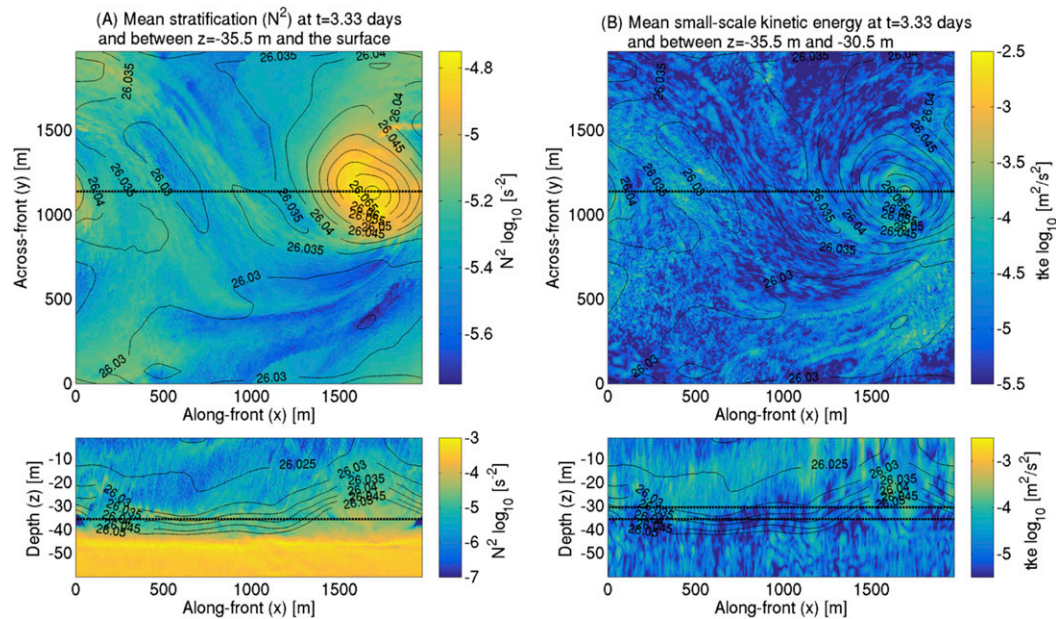
FIG. 4. As in Fig. 3, but at t = 3.33 days, just after the storm is over (see Fig. 1b).

c. Energetics

The contributions of submesoscales and small-scale turbulence to the kinetic energy can be isolated using energy spectra. Here, we focus on the lower part of the mixed layer by presenting spectra at 30-m depth (about 3/4 of H_{ML} after the storm; see Fig. 2a). At this depth, the horizontal and vertical kinetic energy spectra have different slopes at large and small scales (Figs. 5a,b). In addition, the vertical kinetic energy spectra exhibit two local maxima: one at a wavenumber of about 1/1000 cycles per meter (near the fastest growing MLI mode) and one at a wavenumber between 1/50 and 1/100 cycles per meter. This motivates using a cutoff wavenumber k_c = 1/150 cycles per meter, near the local minimum in the vertical kinetic energy spectra (see Fig. 5b), to separate large from small scales.

Large-scale horizontal kinetic energy dominates the total kinetic energy in the wind-forced front. It grows during the storm and decays to about 25% of its late-storm maximum after the end of the storm (Fig. 5c). In contrast, large-scale horizontal kinetic energy rises only slightly in the front forced by a weak air–sea buoyancy flux and decays during forcing in the front forced by a strong air–sea buoyancy flux. Hence, the total kinetic energy is more than 10 times larger during the storm in the wind-forced front than in any of the other three simulations (Figs. 5c,d).

Large-scale vertical kinetic energy is about 10 times larger during the storm than before or after the storm in the simulation with a wind-forced front (Fig. 5d), which is qualitatively consistent with earlier studies that show wind enhances submesoscale vertical motions at fronts

(e.g., Mahadevan and Tandon 2006; Thomas et al. 2008). However, the large-scale vertical kinetic energy is also enhanced during the storm in the simulation forced by a strong buoyancy flux (Fig. 5d, dashed red line). Comparing Figs. 5b and 5d, it is evident that the large scales are highly anisotropic at a wind-forced front (blue lines), while strong convective forcing (red lines) causes the flow to become more isotropic (although the large-scale horizontal kinetic energy is still more than 10 times larger than the vertical kinetic energy in this case.)

During the storm, the small-scale turbulent kinetic energy is similar in all three simulations with strong surface forcing (Fig. 5). However, after the storm, small-scale turbulence is less energetic, and small-scale spectral slopes are steeper for the wind-forced front compared to the simulation without the front (Fig. 5), presumably because the submesoscale restratification suppresses small-scale turbulence at 30-m depth in the simulation with the front (see Fig. 4). Yet, small-scale turbulence is more energetic in the large domain during a transition period just after the storm, for example, between days 2.75 and 4 (Figs. 5c,d), which explains why H_{XL} remains deeper than H_{ML} after the storm (Fig. 2a) and suggests that mixing can decouple (in time) from wind forcing at fronts (as in Whitt et al. 2017).

4. Conclusions

It has been known for some time that submesoscales can have a significant impact on stratification and small-scale turbulence in the ocean mixed layer. This work expands our understanding of submesoscale dynamics
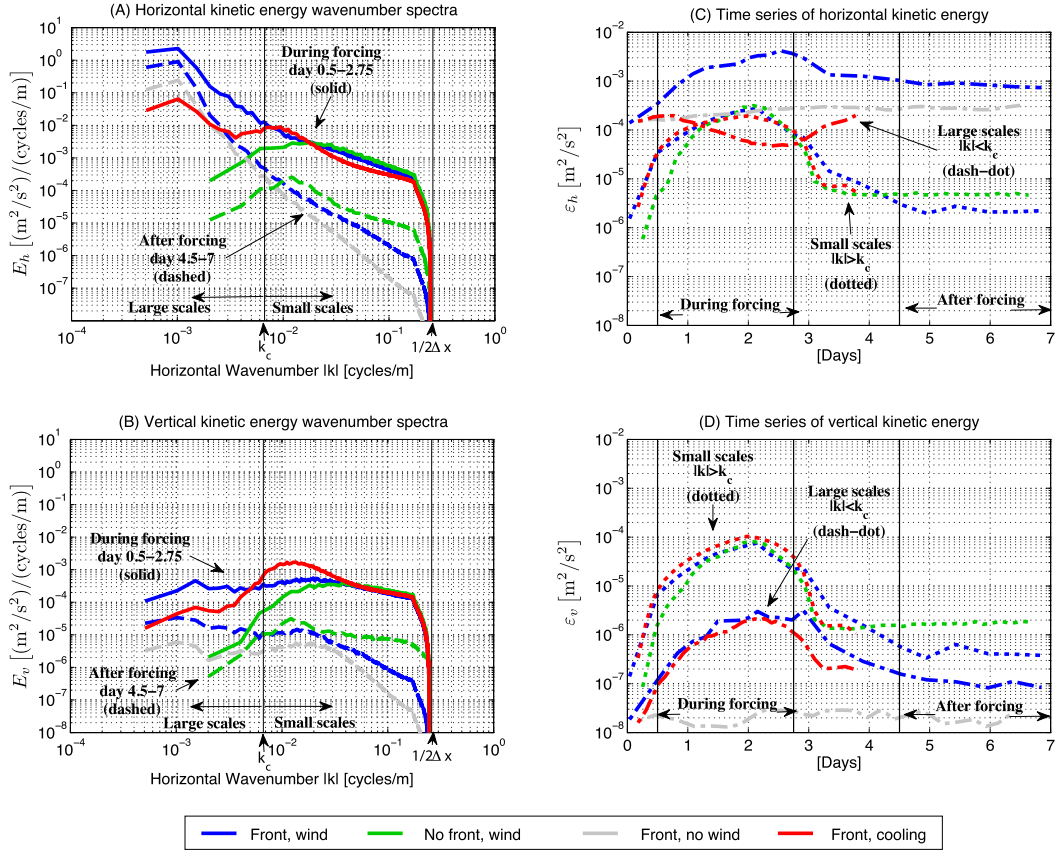
FIG. 5. Time-averaged power spectra of (a) horizontal velocity E_h and (b) vertical velocity E_v at $z = -30$ m as a function of radial horizontal wavenumber $|k_h|$. Time series of (c) horizontal kinetic energy $\mathcal{E}_h = \int E_h dk_h$ and (d) vertical kinetic energy $\mathcal{E}_v = \int E_v dk_h$ in the wind-forced front (blue), the strong buoyancy flux–forced front (red), the weak buoyancy flux–forced front (gray), and the wind-forced domain without a front (green). The wavenumber spectra in (a) and (b) are averaged during the storm ($0.5 < t < 2.75$ days, solid) and after the storm ($4.5 < t < 7$ days, dashed lines). The kinetic energy in (c) and (d) is integrated over small scales (dotted), that is, over wavenumbers $|k_h| > k_c$ where $k_c = 1/150$ cycles per meter, and large scales (dashed–dotted), that is, $|k_h| < k_c$. Several lines are omitted: solid gray lines are omitted from (a) and (b) and dotted gray lines are omitted from (c) and (d) because there is no storm event in that simulation. Dashed red lines are omitted from (a) and (b) because the simulation is not run for the poststorm period. Finally, dashed–dotted green lines are omitted from (c) and (d) because the magnitude is low.

by presenting high-resolution large-eddy simulations that elucidate the interaction between submesoscales and small-scale turbulence during the life cycle of a midlatitude storm. We find that submesoscales persist and even grow during strong winds. Contrary to existing theory and simulation results (Mahadevan et al. 2010), which suggest that submesoscale restratification should be overwhelmed by the destratifying effects of the Ekman buoyancy flux, our simulations show that submesoscales maintain strong mean stratification in the mixed layer even in the midst of strong downfront winds. Despite the strong mean stratification, small-scale turbulence intermittently penetrates to the mixed layer base because of strong modulation of mixed layer stratification on submesoscales. The small-scale turbulent

kinetic energy is enhanced in regions of relatively weak stratification, both during and after the storm.

The persistence of strong, stable stratification during the storm, first reported by Rumyantseva et al. (2015) and confirmed here by the LES, challenges the prevailing description of submesoscales. Recent work has framed the description of the mixed layer depth and stratification as a competition between restratification by submesoscales associated with horizontal density gradients and mixing by small-scale turbulence associated with surface forcing (e.g., Mahadevan et al. 2010, 2012; Bachman and Taylor 2016; Taylor 2016). The results here suggest a more nuanced description where winds simultaneously energize small-scale turbulence and submesoscales. Notably, the submesoscale horizontal kinetic energy is significantly

enhanced during the storm (see Fig. 5b). Despite the enhanced small-scale turbulence and the large destabilizing Ekman buoyancy flux and large values of the mixed layer buoyancy flux ratio R_{ML}, strong stratification persists in localized patches (Fig. 3a). The same level of stratification is not seen in a simulation with the same R_{ML} without wind forcing, suggesting that the enhancement of submesoscale activity by wind forcing is important for the evolution of mixed layer stratification.

These results raise several important questions for future work, including the following: Is MLI enhanced by small-scale ($<1\,\mathrm{km}$) buoyancy gradients and/or strong Ekman shear? Does the domain size constrain the dynamics of the submesoscales? Do surface waves, which are excluded here, modify the results? Finally, how do the results depend on the chosen parameters, including the horizontal and vertical density gradients, the wind stress, and the air–sea buoyancy flux?

Although only one set of parameters is considered here, this set of parameters is typical of the OSMOSIS site (Thompson et al. 2016) and presumably is relevant to other regions of the ocean. Moreover, the simulated strong stratification during the storm is qualitatively consistent with the observed mixed layer stratification at the OSMOSIS site during the September storm (Rumyantseva et al. 2015). Hence, the results, which challenge our current understanding of submesoscale dynamics, could provide insight into typical ocean conditions during the passage of a storm.

REFERENCES

Anderson, P. S., 2009: Measurement of Prandtl number as a function of Richardson number avoiding self-correlation. *Bound.-Layer Meteor.*, **131**, 345–362, doi:10.1007/s10546-009-9376-4.

Bachman, S. D., and J. R. Taylor, 2016: Numerical simulations of the equilibrium between eddy-induced restratification and

vertical mixing. *J. Phys. Oceanogr.*, **46**, 919–935, doi:10.1175/JPO-D-15-0110.1.

Boccaletti, G., R. Ferrari, and B. Fox-Kemper, 2007: Mixed layer instabilities and restratification. *J. Phys. Oceanogr.*, **37**, 2228–2250, doi:10.1175/JPO3101.1.

Buckingham, C. E., and Coauthors, 2016: Seasonality of submesoscale flows in the ocean surface boundary layer. *Geophys. Res. Lett.*, **43**, 2118–2126, doi:10.1002/2016GL068009.

Callies, J., G. Flierl, R. Ferrari, and B. Fox-Kemper, 2016: The role of mixed-layer instabilities in submesoscale turbulence. *J. Fluid Mech.*, **788**, 5–41, doi:10.1017/jfm.2015.700.

Capet, X., J. C. McWilliams, M. J. Molemaker, and A. F. Shchepetkin, 2008: Mesoscale to submesoscale transition in the California Current System. Part I: Flow structure, eddy flux, and observational tests. *J. Phys. Oceanogr.*, **38**, 29–43, doi:10.1175/2007JPO3671.1.

D'Asaro, E., C. Lee, L. Rainville, R. Harcourt, and L. Thomas, 2011: Enhanced turbulence and energy dissipation at ocean fronts. *Science*, **332**, 318–322, doi:10.1126/science.1201515.

Davis, R. E., R. DeSzoeke, D. Halpern, and P. Niiler, 1981: Variability in the upper ocean during MILE. Part I: The heat and momentum balances. *Deep-Sea Res.*, **28A**, 1427–1451, doi:10.1016/0198-0149(81)90091-1.

Dohan, K., and R. E. Davis, 2011: Mixing in the transition layer during two storm events. *J. Phys. Oceanogr.*, **41**, 42–66, doi:10.1175/2010JPO4253.1.

Forryan, A., A. C. Naveira Garabato, K. L. Polzin, and S. Waterman, 2015: Rapid injection of near-inertial shear into the stratified upper ocean at an Antarctic Circumpolar Current front. *Geophys. Res. Lett.*, **42**, 3431–3441, doi:10.1002/2015GL063494.

Fox-Kemper, B., R. Ferrari, and R. Hallberg, 2008: Parameterization of mixed layer eddies. Part I: Theory and diagnosis. *J. Phys. Oceanogr.*, **38**, 1145–1165, doi:10.1175/2007JPO3792.1.

Haine, T. W. N., and J. Marshall, 1998: Gravitational, symmetric, and baroclinic instability of the ocean mixed layer. *J. Phys. Oceanogr.*, **28**, 634–658, doi:10.1175/1520-0485(1998)028<0634:GSABIO>2.0.CO;2.

Hamlington, P. E., L. P. VanRoekel, B. Fox-Kemper, K. Julien, and G. Chini, 2014: Langmuir–submesoscale interactions: Descriptive analysis of multiscale frontal spindown simulations. *J. Phys. Oceanogr.*, **44**, 2249–2272, doi:10.1175/JPO-D-13-0139.1.

Hoskins, B., 1974: The role of potential vorticity in symmetric stability and instability. *Quart. J. Roy. Meteor. Soc.*, **100**, 480–482, doi:10.1002/qj.49710042520.

Kaltenbach, H.-J., T. Gerz, and U. Schumann, 1994: Large-eddy simulation of homogeneous turbulence and diffusion in stably stratified shear flow. *J. Fluid Mech.*, **280**, 1–40, doi:10.1017/S0022112094002831.

Klein, P., and G. Lapeyre, 2009: The oceanic vertical pump induced by mesoscale and submesoscale turbulence. *Annu. Rev. Mar. Sci.*, **1**, 351–375, doi:10.1146/annurev.marine.010908.163704.

Lapeyre, G., P. Klein, and B. L. Hua, 2006: Oceanic restratification forced by surface frontogenesis. *J. Phys. Oceanogr.*, **36**, 1577–1590, doi:10.1175/JPO2923.1.

Large, W. G., and G. Crawford, 1995: Observations and simulations of upper-ocean response to wind events during the ocean storms experiment. *J. Phys. Oceanogr.*, **25**, 2831–2852, doi:10.1175/1520-0485(1995)025<2831:OASOUO>2.0.CO;2.

——, J. C. McWilliams, and P. P. Niiler, 1986: Upper ocean thermal response to strong autumnal forcing of the Northeast

Pacific. *J. Phys. Oceanogr.*, **16**, 1524–1550, doi:10.1175/1520-0485(1986)016<1524:UOTRTS>2.0.CO;2.

——, ——, and S. C. Doney, 1994: Oceanic vertical mixing: A review and a model with a nonlocal boundary layer parameterization. *Rev. Geophys.*, **32**, 363–403, doi:10.1029/94RG01872.

Lévy, M., P. Klein, and A.-M. Treguier, 2001: Impact of submesoscale physics on production and subduction of phytoplankton in an oligotrophic regime. *J. Mar. Res.*, **59**, 535–565, doi:10.1357/002224001762842181.

Mahadevan, A., and A. Tandon, 2006: An analysis of mechanisms for submesoscale vertical motion at ocean fronts. *Ocean Modell.*, **14**, 241–256, doi:10.1016/j.ocemod.2006.05.006.

——, ——, and R. Ferrari, 2010: Rapid changes in mixed layer stratification driven by submesoscale instabilities and winds. *J. Geophys. Res.*, **115**, C03017, doi:10.1029/2008JC005203.

——, E. D'Asaro, C. Lee, and M. J. Perry, 2012: Eddy-driven stratification initiates North Atlantic spring phytoplankton blooms. *Science*, **337**, 54–58, doi:10.1126/science.1218740.

McWilliams, J., 2016: Submesoscale currents in the ocean. *Proc. Roy. Soc. London*, **A472**, 20160117, doi:10.1098/rspa.2016.0117.

Munk, W., L. Armi, K. Fischer, and F. Zachariasen, 2000: Spirals on the sea. *Proc. Roy. Soc. London*, **A456**, 1217–1280, doi:10.1098/rspa.2000.0560.

Niiler, P. P., and E. B. Kraus, 1977: One-dimensional models of the upper-ocean. *Modeling and Prediction of the Upper Layers of the Ocean*, E. B. Kraus, Ed., Pergamon Press, 143–172.

Özgökmen, T. M., A. C. Poje, P. F. Fischer, and A. C. Haza, 2011: Large eddy simulations of mixed layer instabilities and sampling strategies. *Ocean Modell.*, **39**, 311–331, doi:10.1016/j.ocemod.2011.05.006.

Pollard, R. T., P. B. Rhines, and R. Thompson, 1972: The deepening of the wind-mixed layer. *Geophys. Fluid Dyn.*, **4**, 381–404, doi:10.1080/03091927208236105.

Price, J. F., C. N. K. Mooers, and J. C. Van Leer, 1978: Observation and simulation of storm-induced mixed-layer deepening. *J. Phys. Oceanogr.*, **8**, 582–599, doi:10.1175/1520-0485(1978)008<0582:OASOSI>2.0.CO;2.

Rumyantseva, A., N. Lucas, T. Rippeth, A. Martin, S. C. Painter, T. J. Boyd, and S. Henson, 2015: Ocean nutrient pathways associated with the passage of a storm. *Global Biogeochem. Cycles*, **29**, 1179–1189, doi:10.1002/2015GB005097.

Shcherbina, A. Y., E. A. D'Asaro, C. M. Lee, J. M. Klymak, M. J. Molemaker, and J. C. McWilliams, 2013: Statistics of vertical vorticity, divergence, and strain in a developed submesoscale turbulence field. *Geophys. Res. Lett.*, **40**, 4706–4711, doi:10.1002/grl.50919.

Skyllingstad, E., and R. Samelson, 2012: Baroclinic frontal instabilities and turbulent mixing in the surface boundary layer. Part I: Unforced simulations. *J. Phys. Oceanogr.*, **42**, 1701–1715, doi:10.1175/JPO-D-10-05016.1.

——, J. Duncombe, and R. Samelson, 2017: Baroclinic frontal instabilities and turbulent mixing in the surface boundary layer. Part II: Forced simulations. *J. Phys. Oceanogr.*, doi:10.1175/JPO-D-16-0179.1, in press.

Smith, K. M., P. E. Hamlington, and B. Fox-Kemper, 2016: Effects of submesoscale turbulence on ocean tracers. *J. Geophys. Res. Oceans*, **121**, 908–933, doi:10.1002/2015JC011089.

Stamper, M., and J. Taylor, 2016: The transition from symmetric to baroclinic instability in the Eady model. *Ocean Dyn.*, **67**, 65–80, doi:10.1007/s10236-016-1011-6.

Stone, P. H., 1966: On non-geostrophic baroclinic stability. *J. Atmos. Sci.*, **23**, 390–400, doi:10.1175/1520-0469(1966)023<0390:ONGBS>2.0.CO;2.

Taylor, J. R., 2008: Numerical simulations of the stratified oceanic bottom boundary layer. Ph.D. dissertation, University of California, San Diego, 229 pp.

——, 2016: Turbulent mixing, restratification, and phytoplankton growth at a submesoscale eddy. *Geophys. Res. Lett.*, **43**, 5784–5792, doi:10.1002/2016GL069106.

——, and R. Ferrari, 2010: Buoyancy and wind-driven convection at mixed layer density fronts. *J. Phys. Oceanogr.*, **40**, 1222–1242, doi:10.1175/2010JPO4365.1.

Thomas, L. N., A. Tandon, and A. Mahadevan, 2008: Submesoscale processes and dynamics. *Ocean Modeling in an Eddying Regime*, Geophys. Monogr., Vol. 177, Amer. Geophys. Union, 17–37, doi:10.1029/177GM04.

——, J. M. Taylor, R. Ferrari, and T. M. Joyce, 2013: Symmetric instability in the Gulf Stream. *Deep-Sea Res. II*, **91**, 96–110, doi:10.1016/j.dsr2.2013.02.025.

——, ——, E. A. D'Asaro, C. M. Lee, J. M. Klymak, and A. Shcherbina, 2016: Symmetric instability, inertial oscillations, and turbulence at the Gulf Stream front. *J. Phys. Oceanogr.*, **46**, 197–217, doi:10.1175/JPO-D-15-0008.1.

Thompson, A. F., A. Lazar, C. Buckingham, A. C. Naveira-Garabato, G. M. Damerell, and K. J. Heywood, 2016: Open-ocean submesoscale motions: A full seasonal cycle of mixed layer instabilities from gliders. *J. Phys. Oceanogr.*, **46**, 1285–1307, doi:10.1175/JPO-D-15-0170.1.

Thomsen, S., T. Kanzow, F. Colas, V. Echevin, G. Krahmann, and A. Engel, 2016: Do submesoscale frontal processes ventilate the oxygen minimum zone off Peru? *Geophys. Res. Lett.*, **43**, 8133–8142, doi:10.1002/2016GL070548.

Whitt, D. B., 2017: Data for "Energetic submesoscales maintain strong mixed layer stratification during an autumn storm." Figshare, accessed 26 September 2017, doi:10.6084/m9.figshare.c.3816175.v1.

——, J. R. Taylor, and M. Lévy, 2017: Synoptic-to-planetary scale wind variability enhances phytoplankton biomass at ocean fronts. *J. Geophys. Res. Oceans*, **122**, 4602–4633, doi:10.1002/2016JC011899.